Manuscript version: Accepted 24 February 2021
Elsevier, Journal of Materials Research and Technology
https://doi.org/10.1016/j.jmrt.2021.02.090.

Microstructural and mechanical evaluation of post-processed SS 316L manufactured by laser-based powder bed fusion

H. Sohrabpoor 1, *, V. Salarvand 2 , R. Lupoi 3 , Q. Chu 4 , W. Li 4 , B. Aldwell 3,5, W. Stanley 6 , S. O'Halloran 7 , R. Raghavendra 7 , C.-H. Choi 8 , D. Brabazon
1 1: I-Form, Advanced Manufacturing Research Centre & Advanced Processing Technology Research Centre, School of Mechanical & Manufacturing Engineering, Dublin City University, Dublin, Ireland
2: Department of Material and Metallurgy Carno Ideal Arman Company, Hashtgerd, Iran
3: Department of Mechanical and Manufacturing Engineering, Trinity College Dublin, Dublin, Ireland 4: State Key Laboratory of Solidification Processing, Shaanxi Key Laboratory of Friction Welding Technologies, Northwestern Polytechnical University, Shaanxi, China
5: Nammo Ireland, 15-17 Northwest Business Park, Ballycoolin, Dublin, Ireland.
6: University of Limerick, Irish Composites Centre (IComp), Bernal Institute, Faculty of Science and Engineering, Castletroy, Limerick, Ireland
7: SEAM Research Centre, Department of Engineering Technology, Waterford Institute of Technology, Waterford, Ireland
8: Department of Mechanical Engineering, Stevens Institute of Technology, Hoboken, New Jersey, USA
Email: h.sohrab@outlook.com

Abstract Post-processing is one of the main ways to improve mechanical and microstructural characteristics of stainless steel 316L fabricated by the laser-based powder bed fusion (LPBF) process. In this study, optimized LPBF parameters were used to manufacture SS316L bars. For the post-processing, two main heat treatment strategies have been used, quenching and tempering, with various heating and dwelling conditions. While micro-CT scanning was used to identify the porosity inside the as-built specimen, the microstructures of both as-built and heat-treated specimens were additionally investigated by optical microscopy and scanning electron microscopy (SEM). The tensile test's wrought specimens were obtained at various strain rates of 0.1, 0.01, and 0.001 s-1. A two-dimensional (2D) digital image correlation (DIC) technique and fractography analysis were used to understand the tensile behavior further. The results show that the as-built specimen density level was in the range of 99.993-99.997%, with only extremely small pockets of pores present. The microstructure results show that temperature distribution is the most important factor in the formation of columnar grains (CG). The columnar-shaped grains formed from the edge of the melt pool (MP) in the direction of the laser motion path. The resulting dimensions and form of the cellular structures are presented. The crystal orientation of the specimens was also studied with electron backscatter diffraction (EBSD). The result shows that the fraction of directional grains is relatively small due to a scan rotation and the scanning strategies adopted during the LPBF process. With heating at 1050°C with a dwell time of 40 minutes, followed by quenching in cold water, smaller grain sizes were obtained, meaning longer grain boundaries and major impediments to dislocation motion, leading to better mechanical properties and fracture characteristics over wrought specimens. The results of EBSD and SEM were also correlated with the 2D DIC test results.

Keywords: Laser based powder bed fusion; Stainless steel 316L; Strain rate; Quenching; Heat treatment.

Please cite this article as: Sohrabpoor H, Salarvand V, Lupoi R, Chu Q, Li W, Aldwell B, Stanley W, O'Halloran S, Raghavendra R, Choi C-H, Brabazon D, Microstructural and mechanical evaluation of post-processed SS 316L manufactured by laser-based powder bed fusion, Journal of Materials Research and Technology, https://doi.org/10.1016/j.jmrt.2021.02.090.

Manuscript version: Accepted 24 February 2021
Elsevier, Journal of Materials Research and Technology
https://doi.org/10.1016/j.jmrt.2021.02.090.

1. Introduction

Laser-based powder bed fusion (LPBF), or selective laser melting, is one of the most popular additive manufacturing techniques for the fabrication of metals and alloys [1]. In this type of additive manufacturing process, a dense metal powder layer is irradiated by a high energy laser (usually Nd: YAG or fiber laser) to fuse the powder, which causes the metal temperature to go as high as 105 °C and the rate of cooling to go as high as 108 °C/s inside the melting pool (MP) [2]. The characteristics of the MP have a significant effect on the mechanical properties of the LPBF processed specimens. It has been reported that the solid grows epitaxially during the initial solidification around MP boundaries [3]. The heat transfer conditions and phenomena will determine the final microstructure following the initial solidification [3]. Depending on the energy transfer (laser power and scan speed), solid metal is formed as a result of thermal gradient among MPs and previously melted layers, which leads to the formation of textures and columnar types of grain in the as-built parts [4]. The laser spot moves relatively fast (e.g., 0 to 1500 mm/s). As a result, the metal powders melt and solidify quickly, which leads to material solidification under non-equilibrium conditions with retained residual thermal stress [5]. This condition is one of the main disadvantages of additive manufacturing, particularly the LPBF process, compared to conventional manufacturing processes such as casting and forging. One of the main grades of austenitic stainless steel is 316L which has a low carbon amount (0.03 wt %) [6]. For SS316L, the rapid solidification and cooling rate during LPBF lead to very fine cellular structures with fine sub-grains with the size of a few hundred nanometers, which is significantly smaller than the size of grain in traditionally solidified SS316L [7–10]. Based on the previous studies [11–13], the LPBF process achieves substantially higher ultimate tensile strength (UTS) and strain at breakage compared to the traditional methods. During the melting process of LPBF, the final products are under the effects of various manufacturing conditions. These conditions significantly impact specimens' internal composition, including the size and shape of the grain and the distribution of material elemental compositions. Heat treatment is usually employed as post-processing to improve the product quality. The post-processing heat treatment can enhance the mechanical properties of parts made by the LPBF process. In the post-processing heat treatment, the specimens are heated up in a furnace to a predefined temperature and for a set dwell time, followed by cooling in a prescribed approach (e.g., quenching or tempering). The metal is typically heated above the recrystallization temperature and then allowed to cool down to room temperature [11]. After the heat treatment, the mechanical performance of steel largely depends on the number of grains and their morphologies. Chen et al. [13] investigated the impact of heat treatment on the morphology and mechanical performance of SS316L specimens fabricated by the arc additive manufacturing process. Their results show that the amount of σ phase in steel effectively increases after the heat treatment at 1000 °C, causing an increase in UTS and yield strength (YS) but a decrease in the elongation percentage. However, the heat treatment ranging between 1100 and 1200 °C eliminates the σ phase. They also found that the longer dwell time at 1200 °C resulted in grain coarsening and transition from columnar to equiaxed grains. Nan et al. [14]investigated the post-processing of 3D-printed parts of SS316L fabricated by LPBF. They found that an increase in the annealing temperature resulted in lower strength, which was related to the instability of thermal conditioning and heat exposure of cell structures in the as-built specimens. Adjusting the heat treatment parameters can control the microstructural and mechanical performance of austenitic stainless steel [15–18]. Ronneberg et al. [19] investigated

Manuscript version: Accepted 24 February 2021
Elsevier, Journal of Materials Research and Technology
https://doi.org/10.1016/j.jmrt.2021.02.090.

the correlation between mechanical behavior and defects in microstructures in heat treatment of LPBF produced SS316L specimens. According to their results, the dislocation density reduces without significant changes in ductility by the heat treatment. Tassioglou et al. [20] found that heat treatment temperature significantly affected the defects and microstructures of SS316L manufactured by LPBF. They concluded that the heat treatment temperature would be a useful parameter to control the hardness of SS316L. Nonetheless, there is still a lack of comprehensive understanding of the effects of the post processing heat treatment parameters, such as mode, temperature, and dwell time, on the microstructures and mechanical properties of the SS316L manufactured by the LPBF process. In this study, the effects of the post-processing heat treatment parameters, including the temperature and dwell time, on the microstructures and mechanical properties of the LPBF-processed SS316L, were investigated.

2. Experimental process

2.1 Precursor powder

Gas-atomized SS316L powder (LPW Technology Ltd, UK) was employed of particles with a mostly spherical shape, having an average size of 27 µm with Gaussian distribution in the range from 15 to 50 µm. Table 1 shows the elemental compositions of the powder provided by the supplier.

Table 1. 316L stainless steel powder chemical compositions

Chemical compositions	C	Mn	N	P	S	Cr	Mo	O	Ni	Si	Cu	Fe
Mass fraction (%)	0.023	0.9	0.09	0.01	0.005	17.7	2.32	0.03	12.7	0.7	0.01	Bal.

2.2 Laser-based powder bed fusion

The SS316L specimens of cylindrical bars with a diameter and length of 10 mm and 60 mm were manufactured with an EOS M280. The LPBF parameters were optimized to minimize porosity and defects such as un-melted or partially melted grains. A laser power, scan speed, and hatch spacing of 195 W, 1083 mm/s, and 90 µm, respectively, were applied for specimen fabrication. The laser source used in the LPBF machine was a discontinuous Yb-Fiber laser of 200 W maximum power with the laser beam's diameter at 75 µm. The build volume was 250 x 250 x 325 mm3, and the powder layer's thickness during the building was set at 20 µm. The manufactured specimens are shown in Fig 1a. The parts were cut off from the bottom supporting plate by wire electric discharge machining (EDM).

2.3. Mechanical and microstructural properties measurement

The cylindrical bars manufactured were further machined to tensile test dog-bone specimens of 20 mm gauge length and narrow section diameter of 5 mm for tensile tests according to ASTM E8/16a. The tensile tests were performed with a Zwick Z5 5kN Universal Testing Machine. A Carbolite Tube Furnace (CTF 3 1600) with Eurotherm Model 3216 controller was used for the post-processing heat treatment. Two-dimensional digital image correlation (DIC) was applied to evaluate the deformation and strain in the heat-treated SS316L, and results were compared to those obtained from wrought SS316L. In order to obtain clear micrographs for the grain size and orientation, the specimens were polished by chemical etchant consisting of 95%

Manuscript version: Accepted 24 February 2021
Elsevier, Journal of Materials Research and Technology
https://doi.org/10.1016/j.jmrt.2021.02.090.

nitric acid and 5% ethanol in volume. This etchant solution was applied on both cross and transverse sections of specimens for around 5 seconds. Fractography and metallography were conducted using a scanning electron microscope (SEM, Carl-Zeiss EVO-LS15) and a 3D digital microscope (Keyence). Fig. 1b presents the optical micrography of the polished specimen. Micro-CT scanning (Fig. 1c) was carried out with a Nikon XTH225 ST, using a rotating target with a voltage of 215 kV and a current of 180 μA. A 0.5-mm thick copper filter was used between the target and the specimen. The resulting voxel size was 6.5 μm in all three axes. Post-image processing was carried out using CT Pro and ImageJ to crop the resulting CT stack and carry out thresholding to identify porosity levels. Specimens for the electron backscatter diffraction (EBSD) measurement in SEM (GeminutesiSEM 500) were prepared using the ion milling method (Leica EM RES102), polished for 2h at the accelerating voltage of 6.5keV

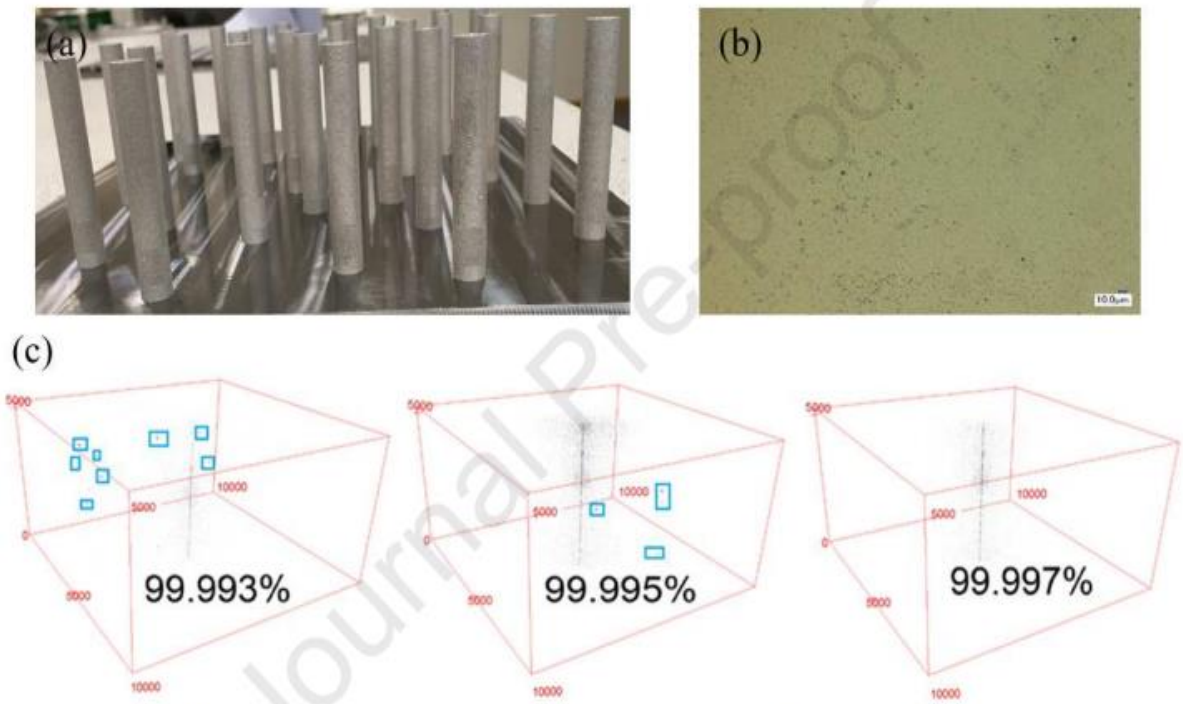

Fig 1. (a) LPBF-processed SS316L specimens, (b) example optical micrograph of a polished cross-section, and (c) examples of the as-build specimens by micro CT scans.

3. Results and discussion

3.1. Microstructures

The as-built parts contained extremely low porosity levels, as shown in the micro CT results (Fig. 1c). The specimens' density levels lie in the range of 99.993-99.997%, with only extremely small pockets of pores present. Fig. 2 shows the optical microscope images of the microstructures of polished and etched specimens.

Manuscript version: Accepted 24 February 2021
Elsevier, Journal of Materials Research and Technology
https://doi.org/10.1016/j.jmrt.2021.02.090.

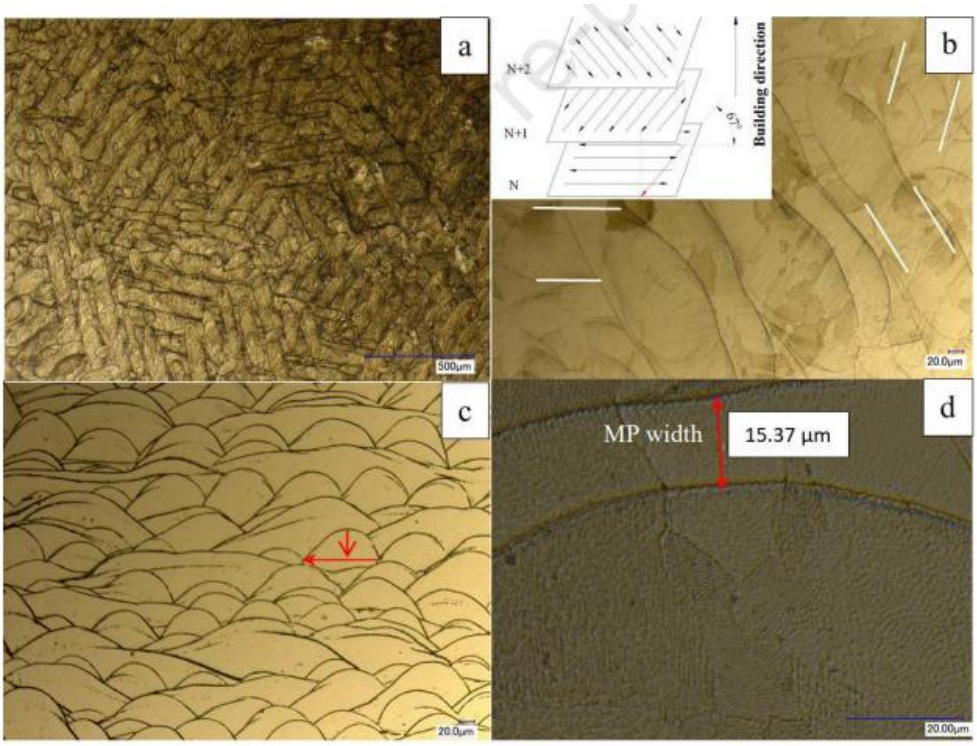

Fig 2. Optical images of the LPBF-processed SS316L, (a) MP tracks - top section of built part, (b) scanning track between layers - top section of build part (inset: schematic of scan strategy), (c) MP - lateral section of built part, and (d) magnified view of MP overlapping.

In the images, the layered structures of the 3D laser-printed specimens can be seen. In Fig. 2a, the orientation of the columnar grains (CG) is shown. The length of the CGs varies between 100 and 250 µm. These grains grow in the direction of the temperature gradient. The columnar-shaped grains formed from MP in the direction of the laser motion path. At higher magnification (Fig. 2b), these orientations are clearly visible. As illustrated in the schematic in Fig. 2b, the laser's scanning path was rotated by 67° in each subsequent layer. This scanning strategy improves the tensile behavior of SS316L specimens [18] significantly compared to other scanning types. As shown in Fig 2c, the ring shape MPs have an average height and width of 80 and 180 µm. Compared to the plan view (Fig 2a), this smaller grain dimension is due to the more rapid solidification resulting from, the higher thermal gradient temperature. As a result of the laser beam center's radial heat transfer, smooth curvilinear boundaries are formed at the grain edge (Fig 2c). Fig 2d shows the MPs' cellular form consisting of multiple overlapping multiple layers of ~15 µm thickness.

Fig. 3 shows different microstructural images of grain structures obtained by SEM. The MP's dimension depends on the exposed laser energy per unit area and per unit time. The MPs formed in a previous scan still have a high temperature to be re-melted by the following laser scan, creating coordinated MPs. The process continues in a repeating and grain intertwining manner. Fig. 3a presents the MP's solidification, showing the columnar type of grains and fine cell structures at the micro-level. The observed cell structure results from the high cooling rate and the non-equilibrium status during the LPBF process. As can be seen from the image, there are different and complex growth directions of columnar grain perpendicular to the building direction (BD), which substantially affects the enhancement of tensile properties. This

Manuscript version: Accepted 24 February 2021
Elsevier, Journal of Materials Research and Technology
https://doi.org/10.1016/j.jmrt.2021.02.090.

phenomenon is one of the main benefits of the LPBF process, unlike the casting and forging, where MPs grow in only one or two directions. The shape of the cell structure is columnar, which is associated with the growth direction of the CGs, as shown in Fig. 3b. The high magnification SEM image (Fig. 3c) shows that the cell structure fits well in each columnal grain along the length direction with a pentagonal or hexagonal shape with a diameter of ~400 nm seen in the transverse direction.

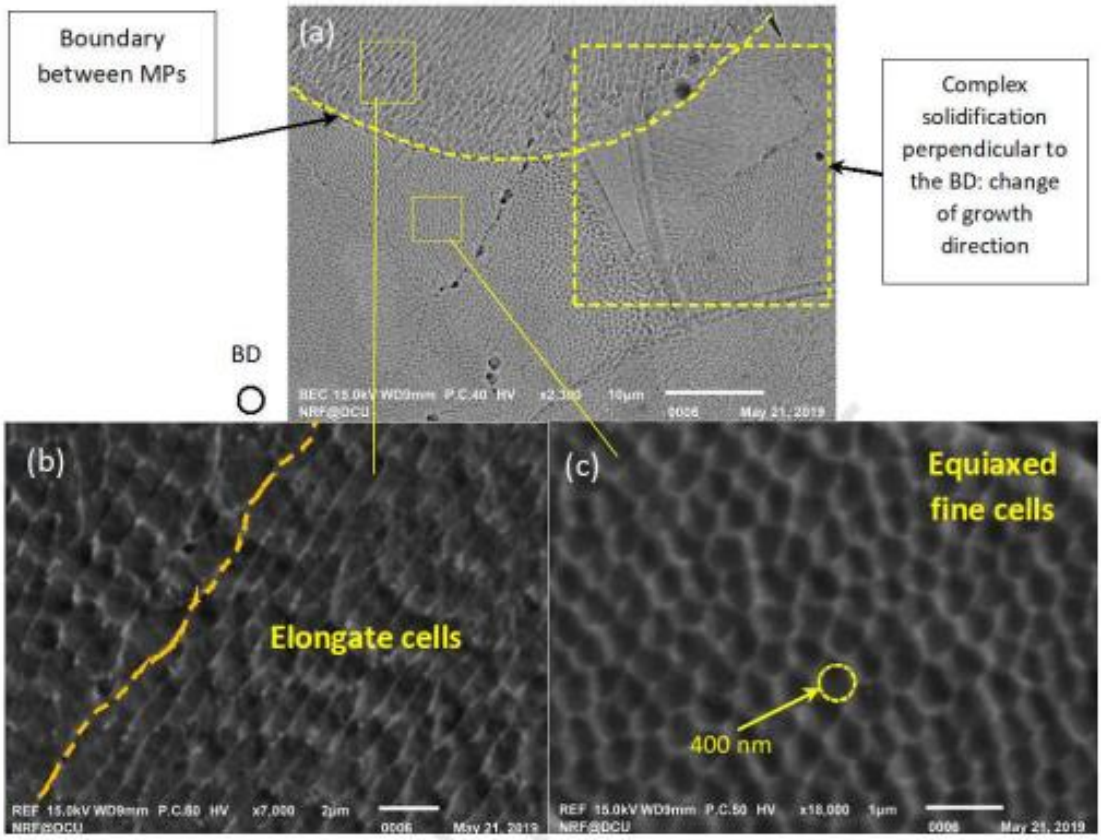

Fig 3. SEM images of polished (etched) specimens showing (a) boundary between melt pools with a mixture of (b) elongated, and (c) equiaxed sub-grains with a size of ~ 0.4 μm.

The fine cellular microstructures are attributed to the high cooling rate from the resulting local quenching process. The formation of these cellular structures is correlated with local compositional alteration due to the mechanism of supercooling. The formed microstructures are related to two thermal factors: the temperature gradient of melt (G) and the rate of solidification (R) [21,22]. The G/R ratio controls the microstructure of the alloy [23,24]. LPBF typically involves a fast-melting process, a non-equilibrium process with a high gradient temperature and cooling/undercooling rates. The typical cooling rate in the LPBF process is 105- 107 ffC/s, highly depending on material properties, part dimension, fluid flow rate, and laser factors [25,26].

3.2. Failure analysis

Fig. 4 shows the two-dimensional DIC which was used to evaluate the deformation and strain in wrought and heat-treated SS316L before failure. Each image is compared against an original

Manuscript version: Accepted 24 February 2021
Elsevier, Journal of Materials Research and Technology
https://doi.org/10.1016/j.jmrt.2021.02.090.

reference image at the start of the test (0 sec). Near the end of the test, some points in the specimen's high strain regions are not correlated. When this occurs, the correlation mode is manually changed to 'incremental'; each image is compared to the previous image instead of the original reference image. For the specimen with the heat treatment at 1050 °C, cracks initiated at 40 s, while the cracks in the specimen with the heat treatment at 900 °C started earlier at 20 s. It indicates that the heat treatment at the higher temperature improved the ductility significantly, which resulted from an increase in the number of grain boundaries (i.e., smaller grain size). On the other hand, at the lower temperature, a recrystallization process can result in larger grains and a decrease in the number of grain boundaries, allowing cracks to grow more quickly, leading to lower ductility.

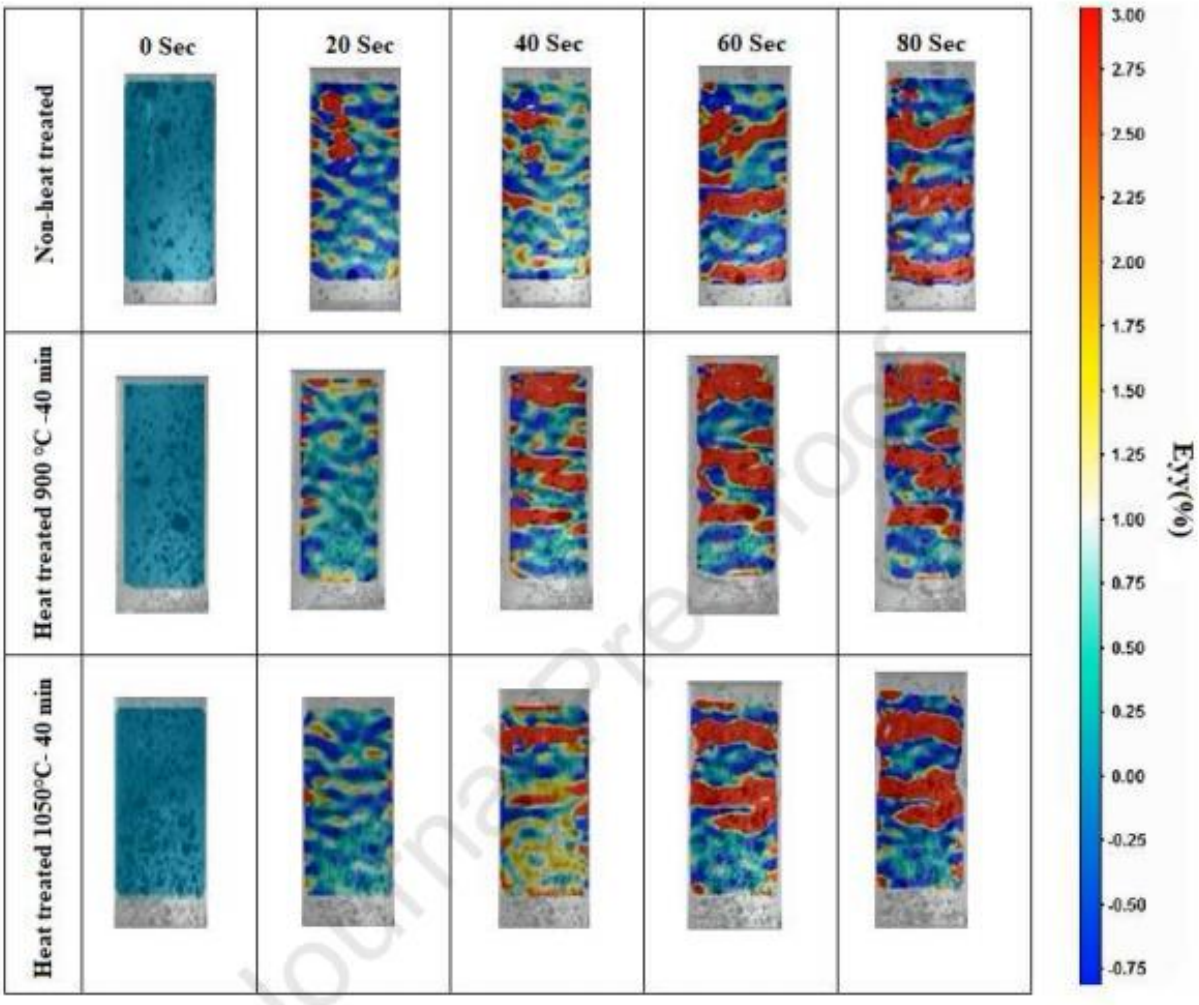

Fig. 4 DIC contour plot, where Eyy is an indicator of true strain rate.

Fig. 5 shows the ultimate tensile strength (UTS) results, break strain, and yield strength of the LPBF-processed SS316L with three different strain rates of 0.1, 0.01. and 0.001 s-1. Fig. 5a-c and e-d show the SEM fractography images of areas of porosity and fracture surfaces at the three different strain rates, respectively. It should be noted that the average dimension of the ductile dimples measured in this study is relatively small compared to those previously reported [27– 29]. The size of dimples is usually in accordance to the extent of intragranular cells. The

Manuscript version: Accepted 24 February 2021
Elsevier, Journal of Materials Research and Technology
https://doi.org/10.1016/j.jmrt.2021.02.090.

size of the dimples shown in Fig 5a, b, and c are from a few hundred nanometers to one micron, which is approximately equal to the size of the intragranular cells [30]. It has been reported that some silicon-rich spherical oxide nano-inclusions can be found [31]. Although the LPBF process was conducted in inert gas, it was probable that a small amount of oxygen remained inside the chamber. When the laser irradiates on the raw powder, the metal's Si element could react with oxygen. Oxides can randomly distribute in the form of spherical nano-inclusions during the cooling and are typically not well bound to the surrounding metal [31].

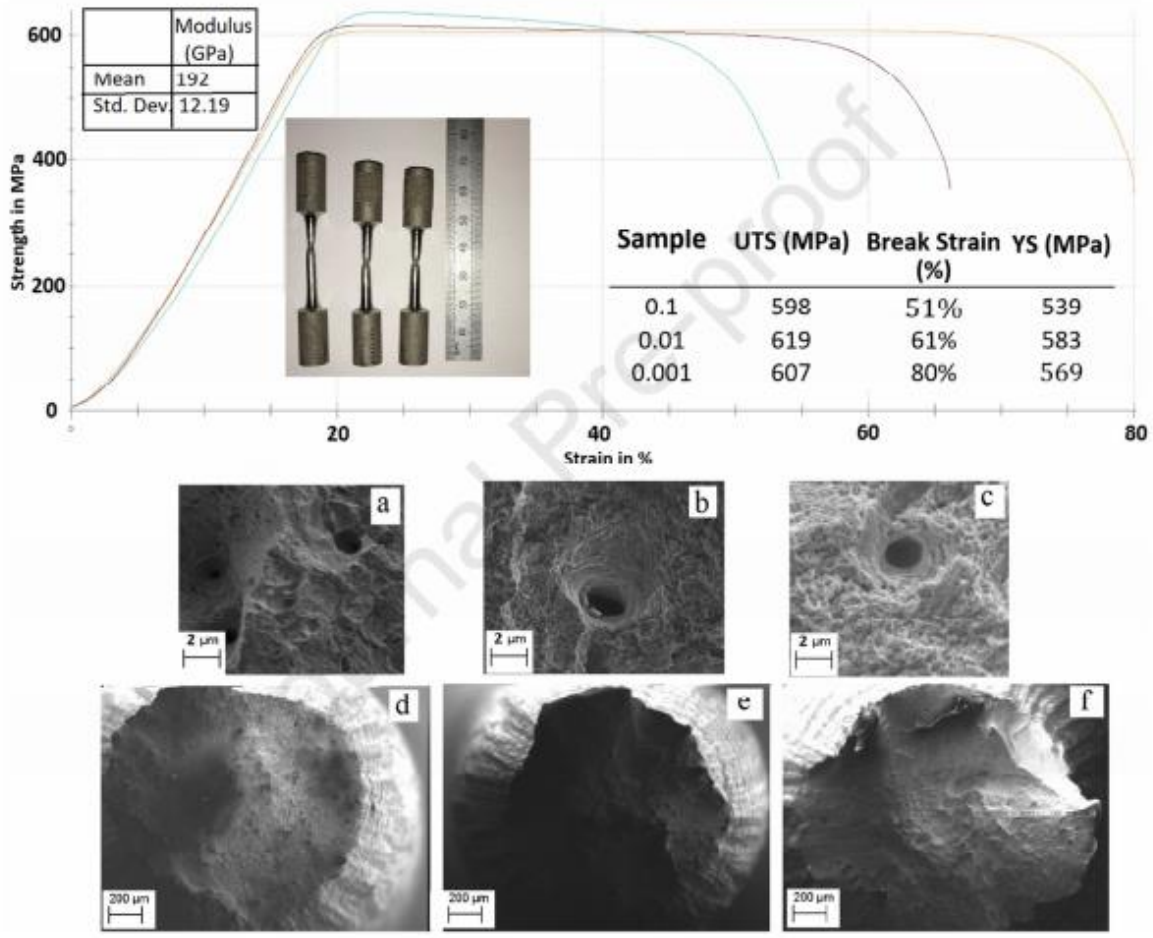

Fig. 5. UTS results, break strain, and yield strength of the LPBF-processed SS316L with three different strain rates of 0.1, 0.01, and 0.001 s-1. SEM fractography of fracture surfaces with porosity at the three different strain rates (a, d) 0.1 s-1, (b, e) 0.01 s-1, and (c, f) 0.001 s^{-1}

The fracture surface morphology of the LPBF SS316L after the tensile test is shown in Fig. 6. The specimens' fracture surface shows ductile fracture with dimples, submicron dimensions, and brittle fracture with protrusions (Fig. 6a). A large number of dimples with sizes ranging from a few hundred nanometers to one micron are noticed on the specimen's fracture surface. The large dimples are likely to be critical areas for the failure of the specimen in the tensile test. As shown in Fig. 6b, an un-melted spherical particle of the powder was found in the large cavity. In the LPBF process, partially melted and un-melted powder granules can remain in the area between MPs. Those particles cause the crater-like voids when pulled in the tensile tests and remain on the fracture surface. By optimizing the processing parameters in LPBF, the

Manuscript version: Accepted 24 February 2021
Elsevier, Journal of Materials Research and Technology
https://doi.org/10.1016/j.jmrt.2021.02.090.

amount of such defects can be minimized, although it is impossible to eliminate them completely. Although the LPBF-processed SS316L has some defects, such as the low-density regions, its mechanical properties, such as UTS are significantly better than those produced by casting and forging. Thus, the LPBF-processed SS316L is usually more resistant to the defects. Fig. 6c shows the cup fracture of wrought specimen under the strain rate of 0.001 s-1. Based on the observed features in this study, the average dimension of dimples of ductile fractures is significantly smaller than those achieved by previous works [2–4,6–10,15,17] on SS 316L produced by the LPBF process.

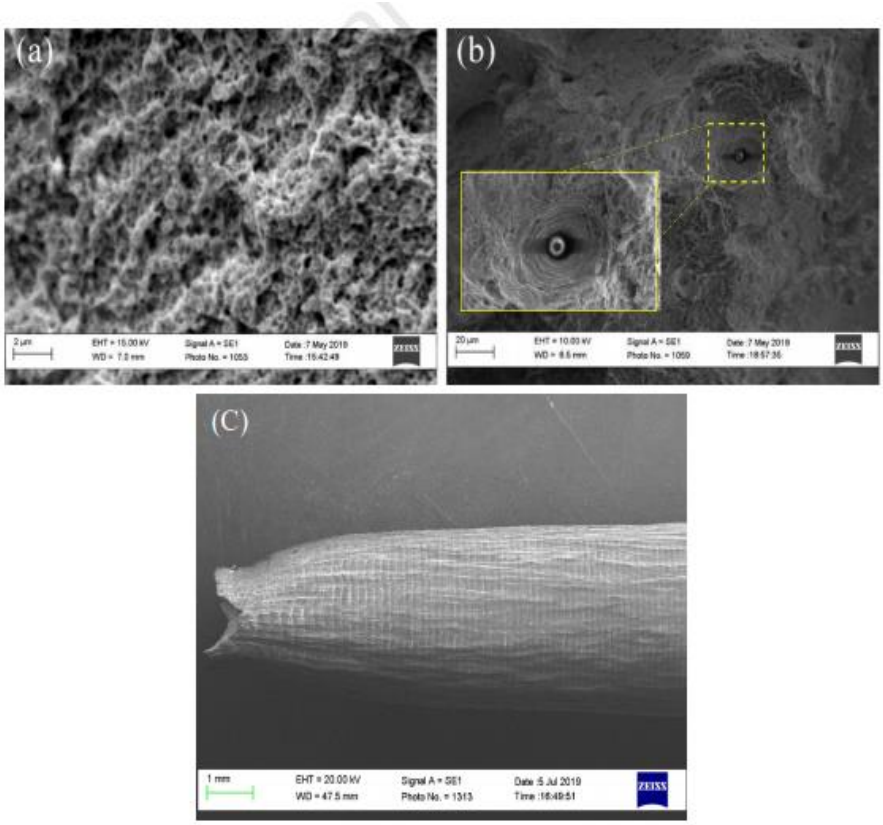

Fig. 6. SEM images of (a) a fracture surface under a strain rate of 0.001 s-1, (b) an un-melted particle, and (c) cup fracture under a strain rate of 0.001 s^{-1}

Fig. 7 shows the SEM images of the fracture surfaces of the as-built and heat-treated specimens in various conditions. Dimples and layered structures are shown on the as-built fracture surfaces (Fig. 7b) and the heat-treated specimen at 900 °C (Fig. 7d). A quasi-cleavage plane, which may indicate the MP boundary, is seen between the layered structures. Un-melted powder particles and large craters were also found on the fracture surfaces. These particles can facilitate crack growth under tensile stress. However, as for the heat-treated specimen's fracture surfaces at 1050 °C (Fig. 7e), craters do not exist. It is attributed to the higher temperature in heat treatment which leads to the closing of the craters. The dimples in the heat-treated wrought specimens are more uniform, with fewer voids than the as-built LPBF specimens. The dimple size of the wrought specimens with heat treatment is between 100 to 300 μm, significantly smaller than that fabricated by traditional processes such as casting and forging.

Manuscript version: Accepted 24 February 2021
Elsevier, Journal of Materials Research and Technology
https://doi.org/10.1016/j.jmrt.2021.02.090.

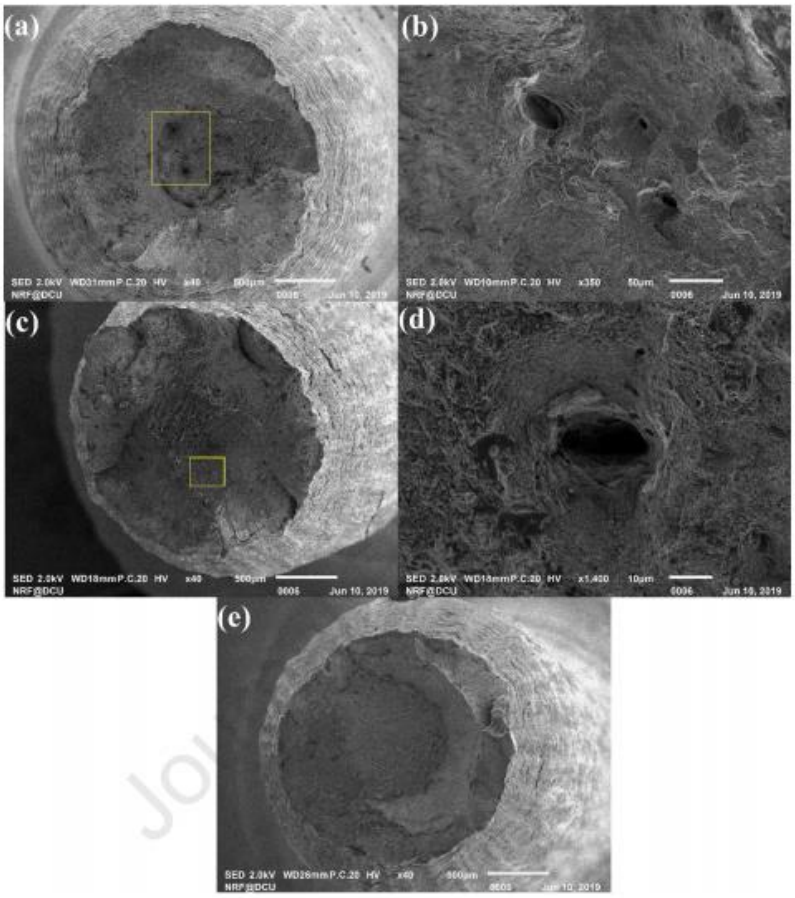

Fig. 7. SEM fractography images of wrought specimens, (a-b) as-built, (c-d) heat-treated at 900°C for 40 minutes, followed by quenching, and (e) heat-treated at 1050°C for 40 minutes, followed by quenching.

3.3. Relationships between mechanical performance and cell structure

When a crack propagates under tensile stress, deformation can be disrupted by the trapping of dislocations and nano-inclusions, which improves the tensile properties of the material. However, the energy required for dislocation motion drops with an increase in the heat-treatment temperature, which decreases the pinning effect of dislocations at grain boundaries in the cellular structures. Based on the fracture surface images, the craters shown on the as-built specimens (Fig. 8a-b) are deep and small, while those on the heat-treated specimens at 900°C (Fig. 8c-d) are large and shallow. When the temperature increases in the process, the number of defects decreases, as confirmed by the results of tensile tests. When the length of the specimen during the tensile test increases, the cross-sectional region reduces, which is correlated with the length increase and reduction in the cross-sectional area of MPs and intragranular cells. Based on the tensile test analysis, crack propagation occurs with failure in the material's weak zone or areas with high-stress concentrations during the tensile tests. Fig. 8a shows cracks alongside MP boundaries. In the microstructure of the LPBF-processed SS316L, there are three main types of boundaries: MPs, intragranular cellular boundaries and grain boundaries [38]. MP boundaries may have less bonding strength than the others since they can contain some porosity resulting in low-density areas. When the specimen reaches its

Manuscript version: Accepted 24 February 2021
Elsevier, Journal of Materials Research and Technology
https://doi.org/10.1016/j.jmrt.2021.02.090.

tensile limit at the weakest regions, such as at an MP boundary, the voids or defects (Fig. 8b) can cause the initial void and crack formation (Fig. 8c).

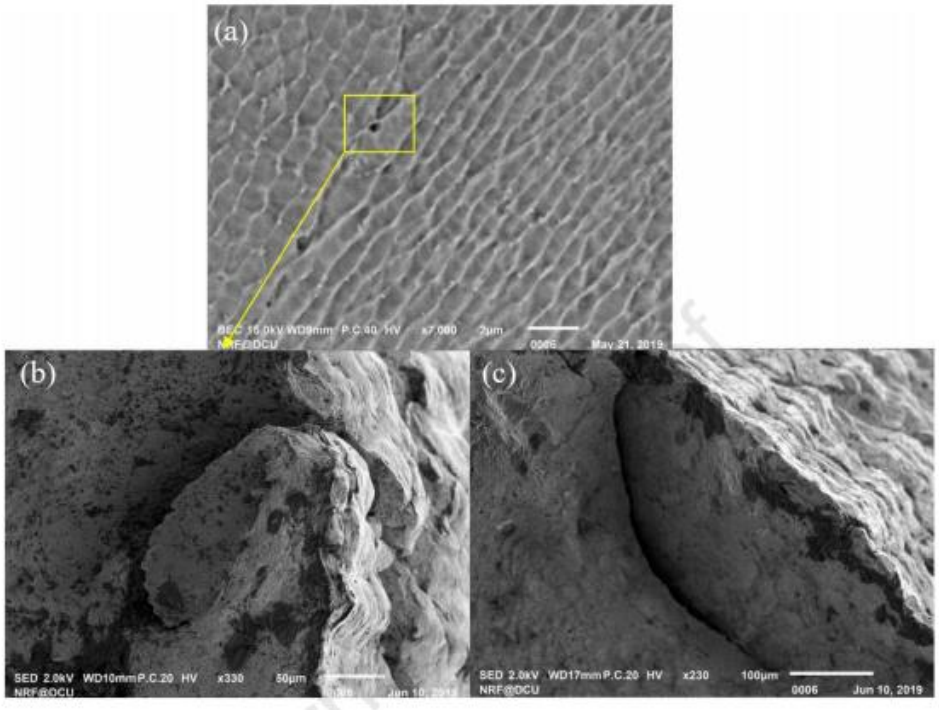

Fig. 8. SEM images of cracks alongside MP boundaries. (a) Grain boundaries, (b) defect, and (c) crack formation.

3.4. EBSD results for the heat-treated and wrought specimens

Fig. 9 shows the crystal orientation maps of the wrought and heat-treated parts evaluated by EBSD analysis. Fig. 9a shows the guide pole figure's image, and the different colors in the following images indicate the different orientations of the grains. Black dotted lines are used to highlight all MP boundaries. In the LPBF process, the texture usually develops due to the directional growth during solidification [32]. However, our results show that the fraction of directional grains (shown in red) is relatively small. This is attributed to the rotation strategy scanning applied during the LPBF process. Fig. 9b illustrates the crystal orientation of the as-built specimen, showing the layered formation of the structure. In contrast, as shown in Fig. 4c, the heat-treated specimen structures followed by cooling at ambient temperature (~25°C) are large and elongated, while the layered structure has not changed. While the smallest grain size of the wrought specimen was measured to be 0.1 μm (Fig 3), the length of the grains of the LPBF-processed specimen was ~0.5 μm after the heat treatment at 900°C for 15 minutes dwelling time, followed by cooling at ambient temperature. The change in grain size affects the ductility. As the grain size decreases, the tensile strength and yield strength generally increase [33,34]. When the cooling was conducted by quenching in cold water instead of at ambient temperature, the layered structure mostly exhibits irregular microstructural orientations, as shown in Fig. 9d. Compared to the case with the heat treatment for 15 minutes followed by ambient cooling, the grains with the extended dwelling time of 40 minutes followed by the ambient cooling showed the larger size and more elongation, as shown in Fig.

Manuscript version: Accepted 24 February 2021
Elsevier, Journal of Materials Research and Technology
https://doi.org/10.1016/j.jmrt.2021.02.090.

9e. This is due to the longer time for grain growth. Fig. 9f shows the structure with the dwelling time of 40 minutes with quenching in cold water. The heat treatment at the elevated temperature of 1050 °C for 40 minutes followed by both the ambient cooling and quenching in cold water was also tested, as shown in Fig. 9g and h, respectively. In ambient cooling, the grain structure does not show any significant changes due to the increase in the temperature, exhibiting the layer-by-layer shape represented by the dashed line in Fig. 4g. In the quenched specimen (Fig. 9h), irregularities in the structure and loss of the layered structure resulted. As the structure becomes disordered and the size of the grain becomes smaller, the dislocation density increases. In such a case, the dislocation is trapped and immobilized along the grain boundaries, which leads to an increase in tensile strength and yield strength [33,34][1,5]. Unlike the quenching in cold water, which leads to finer structure and smaller grain size, cooling in the furnace also provides the grains with more time to grow and expand, similar t Journal Pre-proof o the ambient cooling, as shown in Fig. 9i.

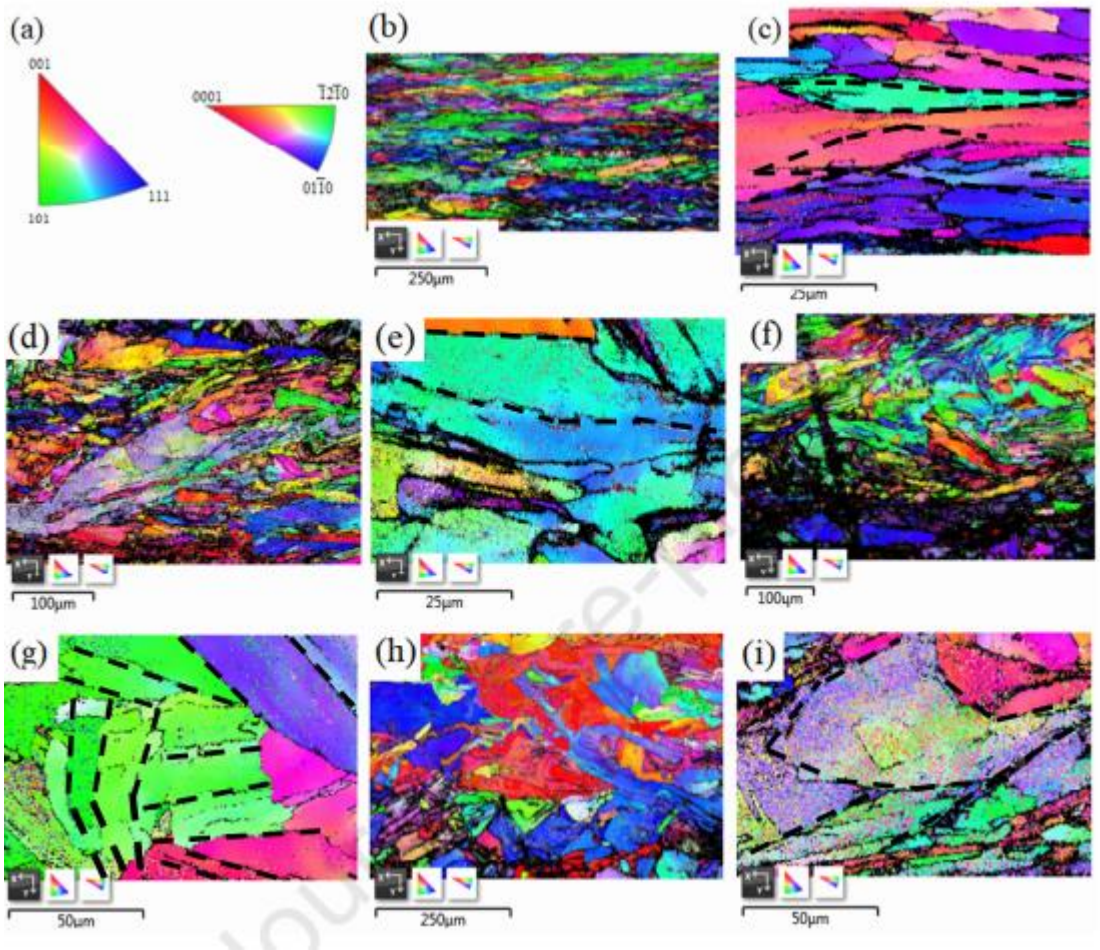

Fig. 9 EBSD orientation analysis. (a) Inverse pole figure, (b) as-built part, (c) heat-treated part at 900°C with 15-minutes dwelling time, followed by no heat treatment for cooling, (d) heat-treated part at 900°C with 15-minutes dwelling time, followed by quenching, (e) heat-treated part at 900°C with 40 minutes dwelling time, followed by no heat treatment, (f) heat-treated part at 900°C with 40 minutes holding time and quenching, (g) heat-treated part at 1050°C with 40 minutes holding time and no heat treatment, (h) heat-treated part at 1050°C with 40 minutes

uses dwelling time and quenching, and (i) heat-treated specimen at 1050°C with 40 minutes dwelling time and cooling in the furnace.

4. Conclusions

This work illustrates how different types of post-processing heat treatment can affect the fractography and crystal orientation characterized by SEM and EBSD microscopies of 316L stainless steel made by laser-based powder bed fusion. Microstructural characterization results with various microscopic techniques for the heat-treated specimens were compared with the as built SS 316L specimen results. A variety of post-processing annealing and quenching conditions up to 1050 °C and 40 minutes were examined. According to the 2D DIC test, at 1050 °C a crack initiated from 40 seconds, unlike the wrought and heat-treated specimens at 900 °C in which cracking started earlier at 20 seconds, meaning that at the highest temperature, ductility improved substantially, which is as a result of an increased number of grain boundaries. Based on the EBSD analysis, heat treatment of specimens at 900 °C and various dwelling times in the tube furnace did not positively affect the mechanical properties. Compared to that, when they quenched at 1050 °C with the 40 minutes dwelling time, the mechanical properties and fractography characteristics improved substantially due to smaller grain size, better uniformity of fused powder, and fewer voids, and defects of the surface fracture.

Acknowledgments

This publication has emanated from research supported by a research grant from Science Foundation Ireland (SFI) under grant number 16/RC/3872 and is co-funded under the European Regional Development Fund.

References

[1] Zhong Y, Liu L, Wikman S, Cui D, Shen Z. Intragranular cellular segregation network structure strengthening 316L stainless steel prepared by selective laser melting. J Nucl Mater 2016;470:170–8. https://doi.org/10.1016/j.jnucmat.2015.12.034.
[2] Liu Y, Yang Y, Mai S, Wang D, Song C. Investigation into spatter behavior during selective laser melting of AISI 316L stainless steel powder. Mater Des 2015;87:797–806. https://doi.org/10.1016/j.matdes.2015.08.086.
[3] Wang D, Song C, Yang Y, Bai Y. Investigation of crystal growth mechanism during selective laser melting and mechanical property characterization of 316L stainless steel parts. Mater Des 2016;100:291–9. https://doi.org/10.1016/j.matdes.2016.03.111.
[4] Suryawanshi J, Prashanth KG, Ramamurty U. Mechanical behavior of selective laser melted 316L stainless steel. Mater Sci Eng A 2017;696:113–21. https://doi.org/10.1016/j.msea.2017.04.058.
[5] Shifeng W, Shuai L, Qingsong W, Yan C, Sheng Z, Yusheng S. Effect of molten pool boundaries on the mechanical properties of selective laser melting parts. J Mater Process Technol 2014;214:2660–7. https://doi.org/10.1016/j.jmatprotec.2014.06.002.
[6] Liverani E, Toschi S, Ceschini L, Fortunato A. Effect of selective laser melting (SLM) process parameters on microstructure and mechanical properties of 316L austenitic stainless steel. J Mater Process Technol 2017;249:255–63.

https://doi.org/10.1016/j.jmatprotec.2017.05.042.
[7] Saeidi K, Gao X, Lofaj F, Kvetková L, Shen ZJ. Transformation of austenite to duplex austenite-ferrite assembly in annealed stainless steel 316L consolidated by laser melting. J Alloys Compd 2015;633:463–9. https://doi.org/10.1016/j.jallcom.2015.01.249.
[8] Casati R, Lemke J, Vedani M. Microstructure and Fracture Behavior of 316L Austenitic Stainless Steel Produced by Selective Laser Melting. J Mater Sci Technol 2016;32:738–44. https://doi.org/10.1016/j.jmst.2016.06.016.
[9] Bartolomeu F, Buciumeanu M, Pinto E, Alves N, Carvalho O, Silva FS, et al. 316L stainless steel mechanical and tribological behavior—A comparison between selective laser melting, hot pressing and conventional casting. Addit Manuf 2017;16:81–9. https://doi.org/10.1016/j.addma.2017.05.007.
[10] Ghayoor M, Lee K, He Y, Chang C hung, Paul BK, Pasebani S. Selective laser melting of austenitic oxide dispersion strengthened steel: Processing, microstructural evolution and strengthening mechanisms. Mater Sci Eng A 2020;788:139532. https://doi.org/10.1016/j.msea.2020.139532.
[11] Niendorf T, Leuders S, Riemer A, Richard HA, Tröster T, Schwarze D. Highly anisotropic steel processed by selective laser melting. Metall Mater Trans B Process Metall Mater Process Sci 2013;44:794–6. https://doi.org/10.1007/s11663-013-9875-z.
[12] Kurzynowski T, Gruber K, Stopyra W, Kuźnicka B, Chlebus E. Correlation between process parameters, microstructure and properties of 316 L stainless steel processed by selective laser melting. Mater Sci Eng A 2018;718:64–73. https://doi.org/10.1016/j.msea.2018.01.103.
[13] Chen X, Li J, Cheng X, Wang H, Huang Z. Effect of heat treatment on microstructure, mechanical and corrosion properties of austenitic stainless steel 316L using arc additive manufacturing. Mater Sci Eng A 2018;715:307–14. https://doi.org/10.1016/j.msea.2017.10.002.
[14] Chen N, Ma G, Zhu W, Godfrey A, Shen Z, Wu G, et al. Enhancement of an additive manufactured austenitic stainless steel by post-manufacture heat-treatment. Mater Sci Eng A 2019;759:65–9. https://doi.org/10.1016/j.msea.2019.04.111.
[15] Sistiaga MLM, Nardone S, Hautfenne C, van Humbeeck J. Effect of heat treatment of 316L stainless steel produced by selective laser melting (SLM). Solid Free Fabr 2016 Proc 27th Annu Int Solid Free Fabr Symp - An Addit Manuf Conf SFF 2016 2016:558–65.
[16] Zitelli C, Folgarait P, Di Schino A. Laser powder bed fusion of stainless steel grades: A review. Metals (Basel) 2019;9. https://doi.org/10.3390/met9070731.
[17] Kamariah MSIN, Harun WSW, Khalil NZ, Ahmad F, Ismail MH, Sharif S. Effect of heat treatment on mechanical properties and microstructure of selective laser melting 316L stainless steel. IOP Conf Ser Mater Sci Eng 2017;257. https://doi.org/10.1088/1757-899X/257/1/012021.
[18] Qi X, Feng H, Liu L. Microstructure and mechanical properties of 316L stainless steel produced by selective laser melting. AIP Conf Proc 2019;2154. https://doi.org/10.1063/1.5125347.
[19] Ronneberg T, Davies CM, Hooper PA. Revealing relationships between porosity, microstructure and mechanical properties of laser powder bed fusion 316L stainless steel through heat treatment. Mater Des 2020;189:108481. https://doi.org/10.1016/j.matdes.2020.108481.

[20] Tascioglu E, Karabulut Y, Kaynak Y. Influence of heat treatment temperature on the microstructural, mechanical, and wear behavior of 316L stainless steel fabricated by laser powder bed additive manufacturing. Int J Adv Manuf Technol 2020;107:1947–56. https://doi.org/10.1007/s00170-020-04972-0.
[21] Ghorbani J, Li J, Srivastava AK. Application of optimized laser surface re-melting process on selective laser melted 316L stainless steel inclined parts. J Manuf Process 2020;56:726–34. https://doi.org/10.1016/j.jmapro.2020.05.025.
[22] Fujii H, Cui L, Tsuji N, Maeda M, Nakata K, Nogi K. Friction stir welding of carbon steels. Mater Sci Eng A 2006;429:50–7. https://doi.org/10.1016/j.msea.2006.04.118.
[23] Samantaray D, Kumar V, Bhaduri AK, Dutta P. Microstructural Evolution and Mechanical Properties of Type 304 L Stainless Steel Processed in Semi-Solid State. Int J M Etallurgical Eng 2013;2013:149–53. https://doi.org/10.5923/j.ijmee.20130202.06.
[24] Liu G, Lu J, Lu K. Surface nanocrystallization of 316L stainless steel induced by ultrasonic shot peening. Mater Sci Eng A 2000;286:91–5. https://doi.org/10.1016/s0921-5093(00)00686-9.
[25] Saeidi K, Gao X, Zhong Y, Shen ZJ. Hardened austenite steel with columnar sub-grain structure formed by laser melting. Mater Sci Eng A 2015;625:221–9. https://doi.org/10.1016/j.msea.2014.12.018.
[26] Riemer A, Leuders S, Thöne M, Richard HA, Tröster T, Niendorf T. On the fatigue crack growth behavior in 316L stainless steel manufactured by selective laser melting. Eng Fract Mech 2014;120:15–25. https://doi.org/10.1016/j.engfracmech.2014.03.008.
[27] Hatami S, Ma T, Vuoristo T, Bertilsson J, Lyckfeldt O. Fatigue Strength of 316 L Stainless Steel Manufactured by Selective Laser Melting. J Mater Eng Perform 2020;29:3183–94. https://doi.org/10.1007/s11665-020-04859-x.
[28] Xu Y, Zhou Z, Li M, He P. Fabrication and characterization of ODS austenitic steels. J Nucl Mater 2011;417:283–5. https://doi.org/10.1016/j.jnucmat.2010.12.155.
[29] Furuya K, Ida M, Miyashita M, Nakamura H. Mechanical properties of F82H/316L and 316L/316L welds upon the target back-plate of IFMIF. J Nucl Mater 2009;386–388:963–6. https://doi.org/10.1016/j.jnucmat.2008.12.259.
[30] Saeidi K, Kvetková L, Lofaj F, Shen Z. Austenitic stainless steel strengthened by the in situ formation of oxide nanoinclusions. RSC Adv 2015;5:20747–50. https://doi.org/10.1039/c4ra16721j.
[31] Lindau R, Möslang A, Schirra M, Schlossmacher P, Klimenkov M. Mechanical and microstructural properties of a hipped RAFM ODS-steel. J Nucl Mater 2002;307–311:769–72. https://doi.org/10.1016/S0022-3115(02)01045-0.
[32] Liu J, Song Y, Chen C, Wang X, Li H, Zhou C, et al. Effect of scanning speed on the microstructure and mechanical behavior of 316L stainless steel fabricated by selective laser melting. Mater Des 2020;186. https://doi.org/10.1016/j.matdes.2019.108355.
[33] Leicht A, Rashidi M, Klement U, Hryha E. Effect of process parameters on the microstructure, tensile strength and productivity of 316L parts produced by laser powder bed fusion. Mater Charact 2020;159:110016. https://doi.org/10.1016/j.matchar.2019.110016.
[34] Wang YM, Voisin T, McKeown JT, Ye J, Calta NP, Li Z, et al. Additively manufactured hierarchical stainless steels with high strength and ductility. Nat Mater 2018;17:63–70. https://doi.org/10.1038/NMAT5021.